Enhanced deglacial carbon transport by Pacific southern-sourced intermediate and mode water

Cyrus Karas [1] ✉, Dirk Nürnberg [2], Fabrice Lambert [3], Gary Shaffer [4] & Frank Lamy [5]

Southern-sourced Antarctic Intermediate Water (AAIW) and Subantarctic Mode Water (SAMW) are currently major sinks of atmospheric CO_2. During the last deglaciation, atmospheric CO_2 levels increased significantly during two specific time periods, Heinrich Stadial 1 (H1) ~18–14.6 ka BP (thousand years ago before present) and the Younger Dryas (YD) ~12.8–11.5 ka BP. Model simulation and proxy data studies suggest that AAIW/SAMW was crucial in explaining these changes during H1 and YD, but its variability and properties in the Southeast Pacific Ocean are still largely unknown. Here, we present records of benthic foraminiferal carbon isotopes, Mg/Ca-based water temperatures, paleosalinity reconstructions, and sortable silt mean grain size variations over the last 30 thousand years from Ocean Drilling Program (ODP) Site 1233, in the Southeast Pacific Ocean, which is bathed in AAIW/SAMW. Our proxy data suggest an increased northward circulation of high pCO_2/ nutrient-enriched AAIW/SAMW during H1 and YD. Our data provides support for AAIW/SAMW as one of the important conduits for deglacial oceanic outgassing in the eastern equatorial Pacific upwelling.

During the present global warming with vast human induced atmospheric CO_2 increase, Antarctic Intermediate Water (AAIW) and Subantarctic Mode Water (SAMW) are major sinks for this anthropogenic CO_2[1]. These water masses are formed in the Southern Ocean in association with upwelling of nutrient enriched deep-water[2,3]. As these waters are undersaturated with respect to heightened atmospheric CO_2 from anthropogenic sources, they absorb CO_2 and transport it along with upwelled nutrients at intermediate depths towards low latitudes[1,3]. In the equatorial Pacific, significant parts of this oceanic stored CO_2 at intermediate water depths enters the Equatorial Undercurrent by way of diapycnal mixing processes and surfaces decades after its entrainment in the high southern latitudes[4,5]. The eastern equatorial Pacific is one of the world's major upwelling regions, where oceanic stored CO_2 is released back into the atmosphere[6,7].

Prior to the industrial revolution, the last deglaciation (~18–11 ka BP) is the most recent time in the Earth's history when global atmospheric CO_2 levels markedly increased by ~80 ppm along with an average global warming of 3–6 °C[8,9]. Deglacial CO_2 increases took place during two short intervals, during ~18–14.5 ka BP known as Heinrich Stadial 1 (H1) and during ~12.8–11.5 ka BP known as the Younger Dryas (YD)[8]. In contrast to the modern, man-made atmospheric CO_2 increase from emissions, this deglacial two-step increase in atmospheric CO_2 resulted from Southern Ocean upwelling (and outgassing) of deep and "old" high pCO_2 and nutrient-enriched water masses that had been isolated from the atmosphere for a long time[10,11].

Several proxy-based studies including $\delta^{13}C$ and radiocarbon activities ($\Delta^{14}C$) of planktonic and benthic foraminifera imply that AAIW/SAMW served as an important conduit of the glacial "old" high pCO_2 water masses from the Southern Ocean toward the eastern

[1]Universidad de Santiago de Chile, Santiago, Chile. [2]GEOMAR Helmholtz Centre for Ocean Research Kiel, Kiel, Germany. [3]Geography Institute, Pontifical Catholic University of Chile, Santiago, Chile. [4]Niels Bohr Institute, University of Copenhagen, Copenhagen, OE, Denmark. [5]Alfred Wegener Institute, Helmholtz Centre for Polar and Marine Research, Bremerhaven, Germany. ✉e-mail: cyrus.karas@usach.cl

Pacific tropical upwelling region and even further north[6,12-19]. Indeed, during deglacial atmospheric CO_2 rise high deglacial surface ocean pCO_2 found in the eastern Pacific equatorial upwelling zone was proposed to partly originate from AAIW/SAMW[6].
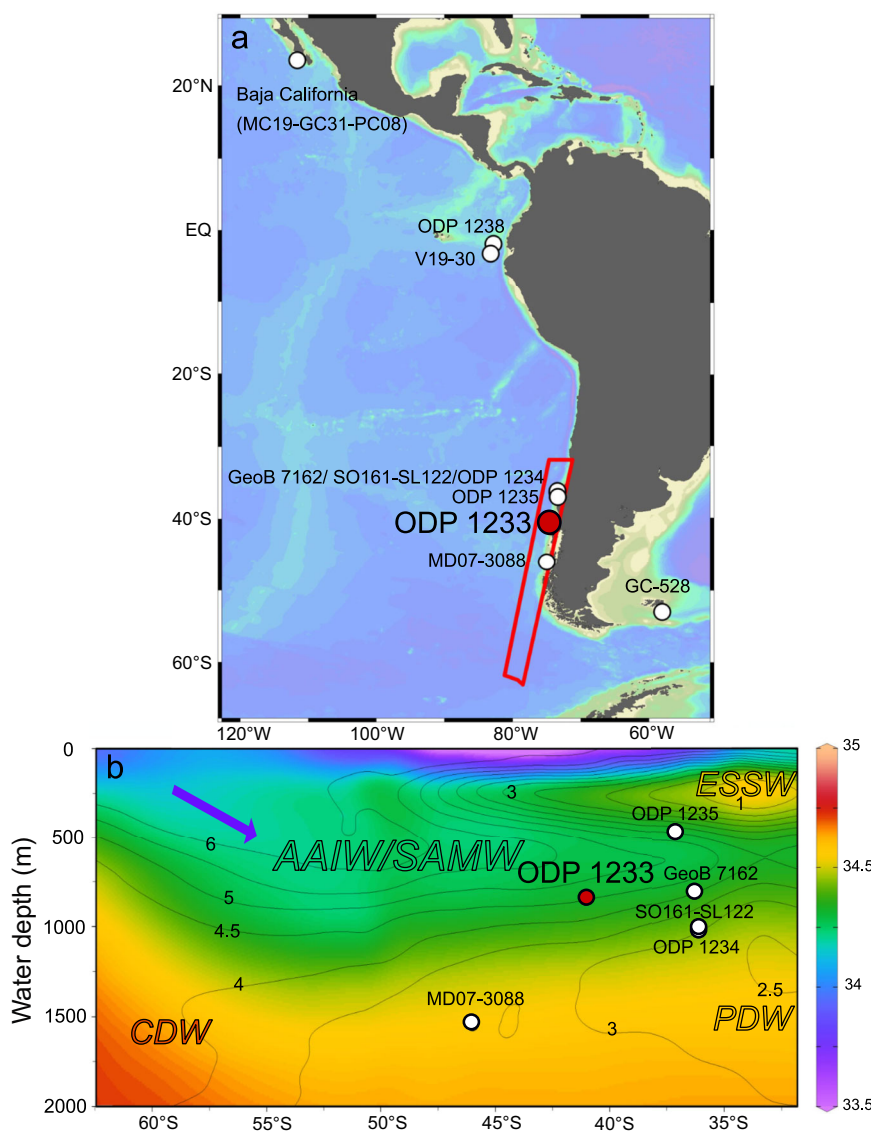
However, the hypothesis that AAIW/SAMW was an important conduit of "old" (high pCO_2 and nutrient-enriched) water during the last deglaciation has yet to be rigorously tested in the Pacific Ocean. Offshore southern Chile, the deglacial AAIW/SAMW evolution (including temperature and salinity) is mostly unknown. Existing datasets for AAIW/SAMW ventilation are either far outside its modern core[20] or are conflicting. For example, increased AAIW circulation was either suggested for the glacial or the deglaciation[21,22], and AAIW as a main conduit of deglacial "old" water masses was rejected and later confirmed[22-24]. To fill this gap, we have developed multi proxy records of up to centennial scale (200 year resolution) from ODP Site 1233 (41°S; 74° 27'W) covering the last 30 kyrs. This Site is close to the major modern formation region of AAIW, which in this area is identical to the densest variety of SAMW[2,25,26]. Its water depth of 838 m puts it at the core of northward flowing AAIW/SAMW (Fig. 1a, b). Hence, we here refer to a combined AAIW/SAMW at our Site, since both water masses are indistinguishable

using geochemical proxies[27] and SAMW was proposed to be a major source for eastern Pacific AAIW[28]. We reconstructed AAIW/SAMW evolution using (1) benthic foraminiferal $\delta^{13}C$ and Ba/Ca as indirect proxies for pCO_2 contents and nutrients, (2) sortable silt mean grain sizes (SS), a direct proxy for paleocurrent speeds and thereby changes in AAIW/SAMW northward flow, and (3) combined benthic $\delta^{18}O$ and Mg/Ca which tracks changes in the AAIW/SAMW temperature and salinity (see Methods and Supplementary Discussion).
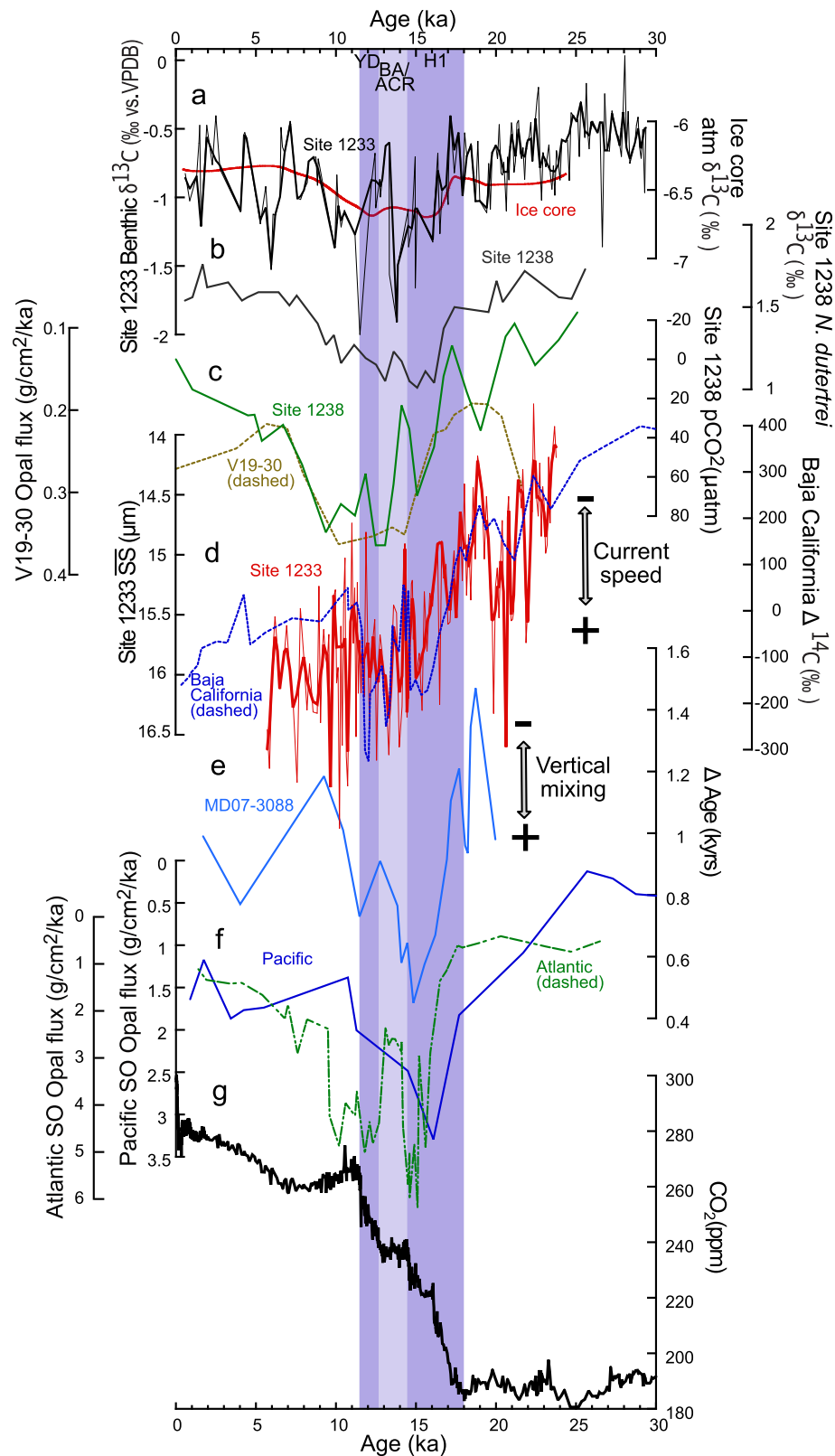
Results and Discussion

South Pacific AAIW/SAMW variability as one important conduit for CO_2 increases in the eastern equatorial Pacific

During the last deglaciation our high-resolution benthic *Uvigerina peregrina* $\delta^{13}C$ record (hereinafter referred to as benthic $\delta^{13}C$) was not affected by surface productivity changes (see Supplementary Discussion and Supplementary Fig. 1). The smoothed record shows a major decrease of ~1.2‰, followed by a second decrease of ~0.6‰ that principally track H1 and YD, when global atmospheric CO_2 levels sharply increased (Fig. 2a, g) and atmospheric $\delta^{13}C$ decreased by ~0.3‰, as recorded in Antarctic ice cores[29] (Fig. 2a).

Fig. 1 | Core locations. a Map showing core locations that are discussed in the eastern Pacific and the Drake Passage. **b** Oceanographic chart of the study area showing salinities (color shading) and oxygen contents (contour lines; in ml/l). The low salinity and high oxygen tongue of modern Antarctic Intermediate Water/ Subantarctic Mode Water (AAIW/SAMW) is indicated as well as Pacific Deep Water (PDW), Equatorial Subsurface Waters (ESSW), and Circumpolar Deep Water (CDW). Studied ODP core Site 1233 is displayed in red, other core sites are in white. Map and chart were created with ODV[81], using data from World Ocean Atlas 2013 (ref. 82,83).

Fig. 2 | Antarctic Intermediate Water/ Subantarctic Mode Water proxy data from Site 1233 in comparison with other records over the last 30 kyr. a Benthic $\delta^{13}C$ from Site 1233 (black, thick line is a 3% weighted smooth made with Kaleida-graph 5.0) and Monte Carlo average of atmospheric $\delta^{13}C$ from two Antarctic ice cores[29] (red). **b** $\delta^{13}C$ of *N. dutertrei* from Site 1238 (ref. [6]; dark grey). **c** pCO2 reconstructions from Site 1238 (ref. [6]; green) and Opal flux from V19-30 (ref. [33]; dashed, brown). **d** Sortable silt mean grain size variations ($\overline{SS}$) (paleocurrent proxy) from Site 1233 (red, thick line is a 3% weighted smooth made with Kaleidagraph 5.0)

and benthic $\Delta^{14}C$ from Baja California sites[16,18] (705 m water depths; dashed, blue). **e** Benthic-planktic ^{14}C age difference from MD07-3088 (1536 m water depth; ref. [24]; light blue). **f** Opal flux from the Pacific sector of the Southern Ocean[38] (blue) and opal flux from the Atlantic sector of the Southern Ocean[10] (dashed, green). **g** Global stack of atmospheric CO_2 reconstructions[8] (black). Shaded purple areas indicate Heinrich Stadial 1 (H1), the Bølling-Allerød /Antarctic Cold Reversal (BA/ACR), and the Younger Dryas (YD).
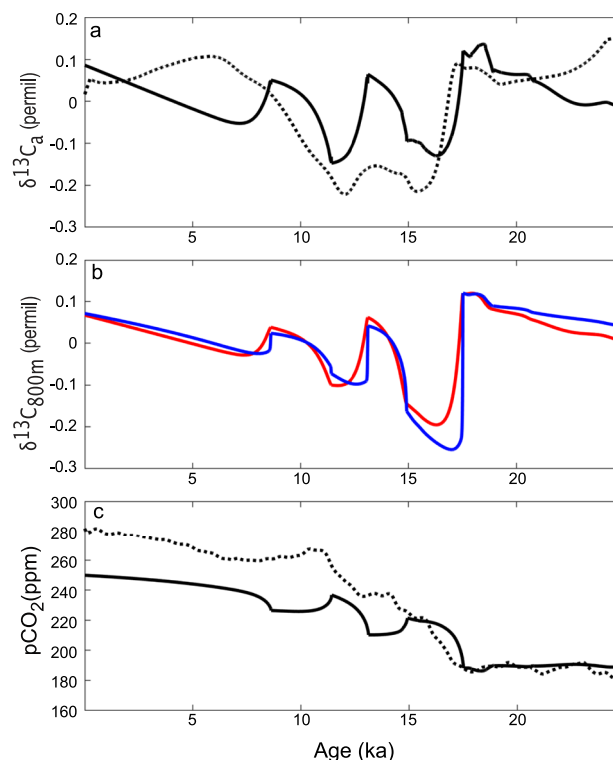
Low atmospheric $\delta^{13}C$ during H1 has been interpreted as a direct consequence of upwelling (and outgassing) of deep, old water masses with low $\delta^{13}C$ and high pCO_2 in the Southern Ocean[29]. The correlation of atmospheric $\delta^{13}C$ (ref. 29) with our benthic $\delta^{13}C$ tightly connects AAIW/SAMW $\delta^{13}C$ with the outgassing of these deep low $\delta^{13}C$ water masses (Fig. 2a). The fact that the amplitude of our benthic $\delta^{13}C$ at 838 m water depth is much larger (2–4 times) than the changes observed in the atmosphere confirms that the low benthic $\delta^{13}C$ is sourced from the deep ocean, and not from the surface ocean as an indirect consequence of outgassing in the Southern Ocean[30].

Multiple lines of evidence support our notion that the low deglacial benthic $\delta^{13}C$ values at AAIW/SAMW depths reflect the entrainment of "old", high pCO_2/ nutrient-enriched water masses into AAIW/SAMW as has been speculated before[6,12–19]. Benthic $\delta^{13}C$ are inversely correlated to Ba/Ca (this study; nutrient proxy) and Rhenium (Re) excess concentrations[21] (proxy for oxygenation) from the same site (see Supplementary Discussion and Supplementary Fig. 1). Further support for our interpretation stems from radiocarbon activities ($\Delta^{14}C$) of benthic foraminifera off the coast of Southern Chile at AAIW/SAMW depths (cores SO161-SL122; GeoB 7162)[22,24] (Fig. 1a, b). Values deviate from the atmospheric $\Delta^{14}C$ record during the deglaciation, and within AAIW/SAMW depths even reaching an extreme low value of ~ −200‰ during H1 (GeoB 7162), marking the presence of "old" water masses[22,24]. In contrast, core sites in the same ocean area but located outside and deeper than modern AAIW/SAMW are within Pacific Deep Water (PDW)[20]. These sites do not show deglacial benthic $\delta^{13}C$ decreases and even point to increases which is in line with a better ventilation of aged glacial PDW[20,24].

Our smoothed $\overline{SS}$ record shows considerable increases from ~14.25 µm to ~16.25 µm during H1 and high values of ~16 µm during YD, suggesting the intensification of AAIW/SAMW-related bottom currents at the intermediate depth core location (Fig. 2d). Such strengthening of AAIW/SAMW circulation together with low oxygen concentrations[21] (high Re) and low benthic $\delta^{13}C$ water (this study; Fig. 2a) is best explained by the entrainment of "old" upwelled Southern Ocean waters into AAIW/SAMW (see also Supplementary Fig. 1). Without this assumption, a stronger circulation would likely lead to increased oxygenation[21], which contradicts the Re excess data.

The postulated acceleration of AAIW/SAMW current speeds is sustained by a model simulation for H1, showing an increased AAIW flow (and an atmospheric CO_2 increase) in response to strengthened and poleward-displaced, Southern Hemisphere westerly winds (SWW)[31]. However, this simulation and a related simulation of atmospheric and oceanic $\delta^{13}C$ did not reproduce our observed negative $\delta^{13}C$ anomalies at AAIW/SAMW depths, but rather in the upper ocean layer[30,31]. Hence, we tested our observed AAIW/SAMW $\delta^{13}C$ anomaly by running a Danish Center for Earth System Science (DCESS) model simulation forced with increased high-latitude ocean (i.e., Southern Ocean) vertical exchange for the H1 and YD periods (see Methods; Supplementary Discussion and Supplementary Fig. 2, 3). The results of the simulation for 800 m water depth qualitatively reproduces our observed negative $\delta^{13}C$ anomalies in the South Pacific AAIW/SAMW, supporting the direct imprint of upwelled old (low $\delta^{13}C$) water masses in the Southern Ocean at AAIW/SAMW depths at Site 1233 (Fig. 3b). In addition, the results of this simulation for atmospheric pCO_2 and $\delta^{13}C$ show considerable agreement in timing and amplitude to the observed pCO_2 and $\delta^{13}C$ changes across H1 and YD (Fig. 3a, c).

Strengthened AAIW/SAMW circulation and low benthic $\delta^{13}C$ between H1 and YD appear quasi-synchronous with the low $\delta^{13}C$ of subsurface-dwelling *N. dutertrei* (habitat depth of ~100 water depth[32]) and increased surface pCO_2 based on boron isotopes from planktic foraminifera at eastern equatorial Pacific upwelling Site 1238 (ref. 6). This is accompanied by high opal accumulation rates at nearby Site V19-30 (ref. 33) (Fig. 2a–d). The synchroneity of events, provides support for the deglacial fueling of this region by increased flow of

Fig. 3 | DCESS model simulation of pCO_2 and $\delta^{13}C$ distributions across the last deglaciation. a Atmospheric observed $\delta^{13}C$ (dashed, black) in comparison to simulated outcome (black). **b** Simulated ocean $\delta^{13}C$ at 800 m depth for low-mid latitudes (0–52°, red) and high latitudes (52–70°, blue). **c** Observed atmospheric pCO_2 (dashed, black) in comparison to simulated outcome (black). For emphasis on the perturbations across the deglaciation, results presented in (**a,b**) have been detrended.

high pCO_2/ nutrient-enriched AAIW/SAMW[6]. Indeed, AAIW/SAMW is in modern times a major southern source for the Pacific Equatorial Undercurrent and is estimated to account for 6–21% of its total transport[5,34]. A significant amount of anthropogenic CO_2 along with nutrients are transported by AAIW/SAMW (including the same density layer we track at Site 1233) into the Equatorial Undercurrent through diapycnal mixing and finally to the surface by upwelling[4,5,35]. Additionally, direct upwelling of large amounts of AAIW/SAMW in the eastern equatorial Pacific was suggested from modern surface $\Delta14C$ data at the Peruvian upwelling and the Costa Rica Dome[36]. Hence, it is plausible that principally during H1 and YD the increased AAIW/SAMW circulation which carried old and high pCO_2 waters would have promoted the enhanced CO_2 outgassing seen at eastern equatorial upwelling Site 1238[6] through one or both of these pathways (Fig. 2a, c, d). Also, other biochemical processes might have played a role for the increased outgassing during the deglacial. For instance, local meso-pelagic nutrient recycling, a recently proposed major source for productivity in low latitudes lead to respiration of organic matter and therefore CO_2 outgassing[37]. Yet it is difficult to quantify this process for the deglaciation, however, we suspect an increase as is simulated for future global warming with rising SST[37]. Deglacial outgassing in the eastern equatorial Pacific upwelling would have been complementary to vast CO_2 outgassing in the Southern Ocean associated with global atmospheric CO_2 increases during H1 and YD[8,10] (Fig. 2g).

The low deglacial *N. dutertrei* $\delta^{13}C$ at ODP Site 1238 (ref. 6) could have been caused by surface exchange with the atmosphere[30]. However, the close correspondence between high opal accumulation rates and increased CO_2 outgassing at the surface, indicates that the *N. dutertrei* $\delta^{13}C$ is associated with upwelling of high pCO2/ nutrient- rich waters[6]. Changes in the intensity of upwelling that could have

impacted the above-described changes could be ruled out at ODP Site 1238 (ref. [6]).

The paleocurrent speed proxy ($\overline{SS}$) record broadly matches the radiocarbon age difference record between planktic and benthic foraminifera from deeper adjacent core MD07-3088 (ref. [24]; Fig. [1]a, b; [2]d, e; 1536 m water depth), a record that reflects water mass stratification changes (small ^{14}C difference = more vertical mixing). The deglacial acceleration of the AAIW/SAMW between H1 and YD is accompanied by an intensification of vertical mixing, and hence a decrease in stratification at core location MD07-3088 (ref. [24]). Apparently, both processes were responding to the intensifying upwelling and mixing of deep-water masses in the Southern Ocean[10,38] (Fig. [2]d–f), forced by increased and southward displaced SWW[10,31].

At the same time there is evidence of reduced intermediate water mass stratification at sites along the Peruvian and Galapagos continental margins inferred from benthic $\delta^{13}C$ and $\delta^{18}O$ records between 400 and 1000 m water depths[12]. It was speculated that AAIW/SAMW warming might have reduced the vertical temperature gradients in the Eastern Pacific, leading to reduced water mass stratification in the eastern equatorial Pacific upwelling region[12].

Our AAIW/SAMW temperature reconstructions at Site 1233 do not show a warming and instead imply rather cool temperatures during H1 and YD. Furthermore, a cooling of ~2 °C is observed at the end of the Bølling-Allerød (BA; ~14.5–12.8 ka BP) which is known in the Southern Hemisphere as the Antarctic Cold Reversal (ACR) (Fig. [4]c). Hence, the increased AAIW/SAMW current speeds during the deglaciation most likely led to an increased contribution of AAIW/SAMW at these intermediate levels northward to the Equatorial Undercurrent and thereby might explain weak intermediate water stratification in the regions cited above.

Our reported changes in proxy records across the last deglaciation could be influenced by vertical changes in the depth of AAIW/SAMW[39]. For instance, a simulated global glacial shallowing of AAIW[40] could move Site 1233 out of the modern core of AAIW/SAMW and under increasing influence of lower Pacific Deep Water (PDW) (Fig. [1]b). Our benthic $\delta^{13}C$ and salinity reconstructions, however, in combination with existing proxy records for oxygenation from Site 1233 and from sites 1235 and 1234 from the upper and lower limit of modern AAIW/SAMW[21] (Fig. [1]a, b) demonstrate that such shifts did not affect Site 1233 and that the changes we observe are instead principally related to changes in the properties and flow speed of AAIW/SAMW itself (see Supplementary Discussion).

South Pacific AAIW/SAMW influence up to Baja California

The close correspondence between our AAIW/SAMW current speed reconstructions and benthic $\delta^{13}C$ with negative benthic $\Delta^{14}C$ excursions at core location MC19-GC31-PC08 off Baja California at 705 m water depth also sheds light on the ongoing controversy regarding the deglacial influence of AAIW there[16,18,19,41–44] (Fig. [1]; [2]a, d). Originally, these negative $\Delta^{14}C$ excursions between H1 and YD were interpreted as the effect of the inflow of "old" Southern Ocean sourced water masses transported via AAIW to this site[16,18,19]. This was contrasted by the view that regional hydrothermal vents might have caused the extreme low $\Delta^{14}C$ off Baja California[43]. A more widespread benthic $\Delta^{14}C$ study in the eastern equatorial upwelling region, although lending support for AAIW as a source for moderate low $\Delta^{14}C$ there, rather favoured North Pacific intermediate waters as a source for low $\Delta^{14}C$ near Baja California, refuting the influence of regional hydrothermal vents[44].

The synchronization in time of our Site 1233 data with near Baja California benthic $\Delta^{14}C$ data clearly supports the original interpretation[16,18,19]. We provide evidence that the increased northward flow of "old" (low $\delta^{13}C$) AAIW/SAMW water masses between H1 and YD could have impacted Baja California causing negative $\Delta^{14}C$ excursions there[16,18] (Fig. [2]a, d). Support comes from neodymium isotope studies from the last deglacial from the same Baja California site (fish teeth)

and the modern (water samples) from a wider area in the North Pacific[42,45]. The deglacial study off Baja California clearly shows a Southern Ocean source during intervals of low $\Delta^{14}C$ excursions[42]. Additionally, the modern-day North Pacific study suggests that AAIW even has a strong impact on North Pacific intermediate waters[45].

SWW as the main driver for AAIW/SAMW changes

Our benthic $\delta^{18}O$ record from Site 1233 largely parallels alkenone-derived SSTs from the same site[46] (age model updated according to our current age model; see Methods) and an Antarctic stacked $\delta^{18}O$ record consisting of five Antarctic ice core cores that reflects changes in surface air temperatures[47] (Fig. [4]a). During H1 SST warming (~18–16 ka BP), there is a dramatic benthic $\delta^{18}O$ decline of ~1.5‰, followed by a plateau of values around 3.5‰ from the end of H1 across BA/ACR and then a decrease again of ~1‰ during the YD warming (Fig. [4]a). These similarities between our benthic $\delta^{18}O$ record and alkenone-derived SST[46] point to nearly synchronous deglacial changes at intermediate and in the surface waters.

The warming periods during H1 and the YD observed in alkenone-derived SST were interpreted as a combination of southward shifts of the SWW and Antarctic temperature increases, that directly affected atmospheric CO_2 increases through upwelling and outgassing in the Southern Ocean[46]. The BA/ACR, however, known as a cooling period in the Southern Hemisphere was described as a warm SST plateau, which did not suggest a rebound of the SWW back to the north[46] (Fig. [4]a).
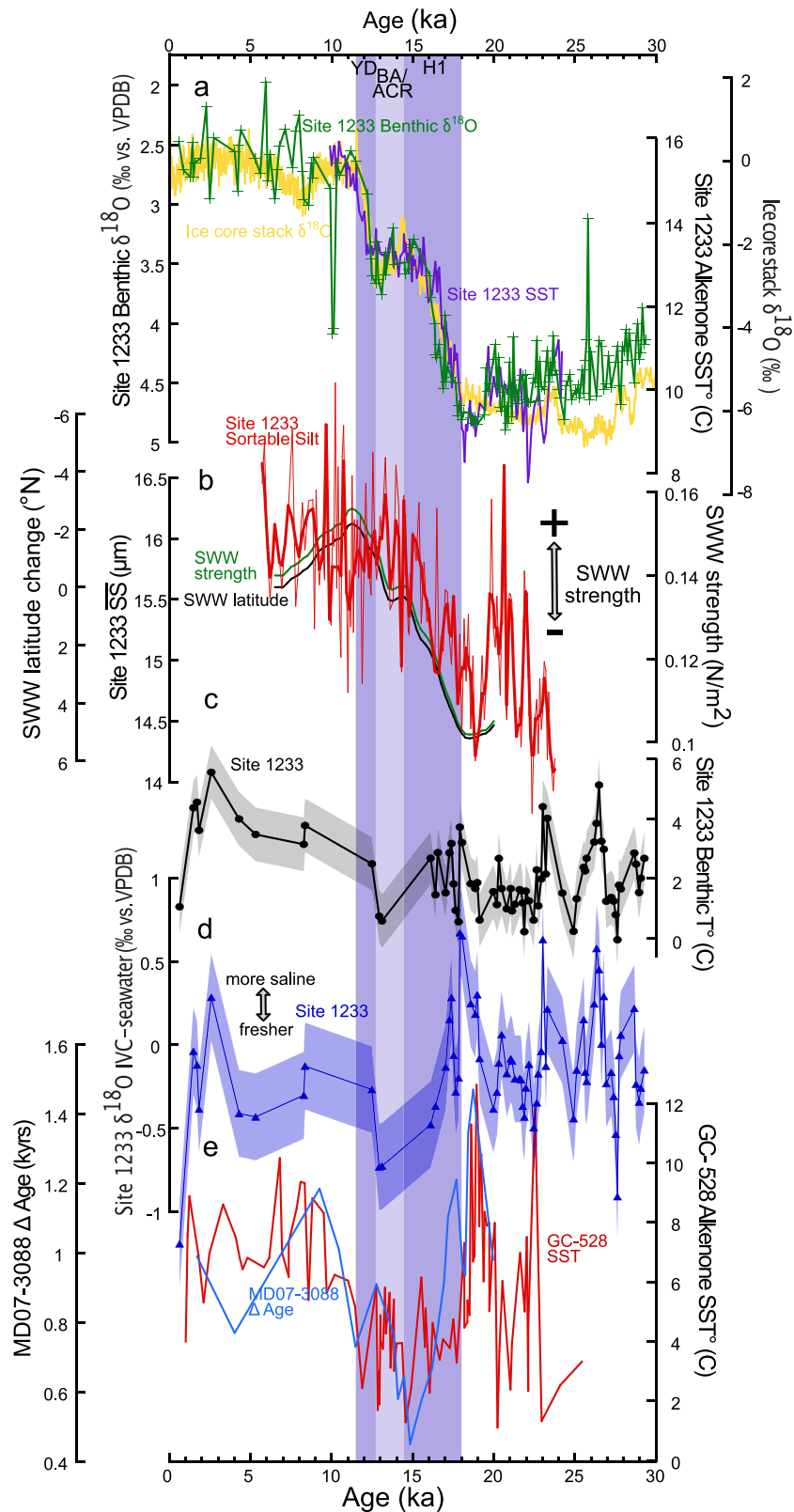
A recent combined model-data study based on available planktic foraminiferal $\delta^{18}O$ records from the Southern Ocean support these deglacial changes in SWW, showing a ~5° poleward shift and ~25% strengthened SWW circulation[48] (Fig. [4]b). As stronger and more southward SWW most likely intensified AAIW formation[31], it makes sense, that the deglacial AAIW/SAMW current speed increases at Site 1233 ($\overline{SS}$) are in broad agreement with these poleward-displaced and strengthened SWW (Fig. [4]a, b).

However, the comparison of our benthic Mg/Ca-derived temperatures ($T_{Mg/Ca}$) with alkenone-derived sea surface temperatures (SST) from the same site[46] shows an opposite development during H1 and at the end of the BA/ACR (Fig. [4]a, c). During H1 (~18 and 16 ka BP), when alkenone-derived SST[46] increased most by ~4 °C, benthic $T_{Mg/Ca}$ stay relatively cold, and at the end of the BA/ACR when benthic $T_{Mg/Ca}$ show a decrease of ~2 °C (Fig. [4]a, c), alkenone derived SST reached a warm plateau ~13 °C (ref. [46]; Fig. [4]a, c).

This lack of deglacial warming of our benthic $T_{Mg/Ca}$ creates an apparent mismatch with our decreasing benthic $\delta^{18}O$ values (Fig. [4]a, c). However, the benthic $\delta^{18}O$ record does not exclusively reflect AAIW/SAMW temperatures, but instead depends on global ice volume, sea water temperature, and salinity. Our benthic $\delta^{18}O_{IVC-seawater}$ record, corrected for these changes in global ice volume and temperature (see Methods) points to a lowering during H1, and at the end of BA/ACR with a total amplitude of ~1.3‰ (freshening), synchronous with relatively cold or cooling of benthic $T_{Mg/Ca}$, at times when the SWWs increased and shifted poleward[48] (Fig. [4]b–d).

Hence, we argue that the freshening with relatively cold AAIW/SAMW temperatures during H1 and at the end of BA/ACR at Site 1233 were mainly driven by these changes in SWW through affecting the source region of AAIW/SAMW. This interpretation is supported by an alkenone-derived SST record from core GC-528 located in the Drake Passage[49] that shows deglacial cooling during the southward shift and strengthening of SWWs[48] that broadly resembles our cold AAIW/SAMW temperatures during H1 and at the end of BA/ACR. (Fig. [4]b, c, e).

Core GC-528 is reasonably representative for the source region of AAIW/SAMW bathing Site 1233 between ~50–60°S, just as modern AAIW formed at Drake Passage-like latitudes contributes to Atlantic Ocean AAIW and Southeast Pacific AAIW/SAMW that flows northward along the coast of Chile[25,50].

The tight interconnection between both ocean regions at different depth levels becomes especially evident by the comparison of our $\delta^{18}O_{IVC\text{-}seawater}$ values with GC-528 alkenone-derived SST[49] (Fig. 4d, e). Warm (cold) periods at GC-528 (ref. [49]) coincide with more saline (fresher) AAIW/SAMW conditions at Site 1233 with notable AAIW/SAMW freshening at the end of BA/ACR.

Previously, it was argued that the deglacial poleward movement of SWW redirected the cold AAIW from the Pacific into the Atlantic, that might explain SST cooling at GC-528 (ref. [49]). However, this would not explain synchronous cool AAIW/SAMW during H1 and cooling during the end of BA/ACR at Site 1233 (Fig. 4c, e).

Fig. 4 | Site 1233 Antarctic Intermediate Water/ Subantarctic Mode Water properties in comparison with changes in Southern Hemisphere westerly winds (SWW) and other proxy data. a Benthic $\delta^{18}O$ from Site 1233 (green, crosses), alkenone-derived sea surface temperatures (SST) from Site 1233 (ref. 46; age model updated according to our current age model; blue), and a stacked Antarctic $\delta^{18}O$ record consisting of five (WAIS Divide, EDML, EDC, Dome Fuji, Talor Dome) Antarctic ice cores[47] (yellow). **b** Reconstructed SWW changes in latitude (black) and strength (gray)[48] and Sortable silt mean grain size variations ($\overline{SS}$) (paleocurrent proxy) from Site 1233 (red, thick line is a 3% weighted smooth made with Kaleidagraph 5.0. **c** Benthic $T_{Mg/Ca}$ from Site 1233 (black, dots) and error band in gray. **d** $\delta^{18}O_{IVC-seawater}$ reconstructions from Site 1233 (dashed blue, triangles) and error band in blue. **e** Alkenone-derived SST from GC- 528 (ref. 49; red) and benthic-planktic ^{14}C age difference from MD07-3088 (ref. 24; blue). Error bands are based on the propagated errors given in the method section. Shaded purple areas indicate Heinrich Stadial 1 (H1), the Bølling-Allerød /Antarctic Cold Reversal (BA/ACR), and the Younger Dryas (YD).

Alternatively, we suggest that strengthening and poleward migration of the SWW enhanced upwelling of cold, deep-water masses and mixing between the polar and the subantarctic fronts nearby GC-528 that caused sea surface cooling in the AAIW/SAMW formation area, consequently affecting AAIW/SAMW temperatures at Site 1233. This cooling effect through upwelling/mixing is evidenced by the synchronous correlation between vertical mixing at MD07-3088 (ref. 24) and alkenone-derived SST at GC-528 (ref. 49) (Fig. 4e). Warm glacial alkenone-derived SST occurred when water masses were stratified, and SST dropped when the stratification decreased during the deglaciation. A general surface cooling effect from the Southern Hemisphere during the final BA/ACR, cannot be ruled out for having indirectly amplified AAIW/SAMW cooling at Site 1233, but seems rather unlikely, as the BA/ACR was not characterized as a surface cooling period at this Site[46]. The high SST during the glacial at GC-528 (ref. 49) could have been amplified by regional meltwater stratification that might explain higher amplitudes there in comparison to Site 1233 AAIW/SAMW temperatures (Fig. 4c, e).

The freshening of AAIW/SAMW during H1 and at the end of BA/ACR at Site 1233 is best explained by increased freshwater input into the AAIW/SAMW formation area, most likely caused by increased precipitation rates due to the southward shift of the SWWs[12,51]. In particular, during H1, this freshening was likely amplified by melting of sea ice or icebergs through vast Antarctic warming[12,51]. During this time, increased sea-ice transport from strengthened SWWs likely intensified AAIW/SAMW formation rates[52]. The formation of relatively fresh AAIW/SAMW during H1 and at the end of BA together with deep upwelling is not unlike the situation in the modern ocean, whereby upwelled relatively salty, Circumpolar Deep Water is transformed in part into relatively fresh AAIW/SAMW[52].

We reconstructed Southeast Pacific AAIW/SAMW properties close to its formation area at ODP Site 1233. Our benthic foraminiferal $\delta^{13}C$ and sortable silt mean grain sizes ($\overline{SS}$) showed prominent $\delta^{13}C$ decreases and a strengthened northward AAIW/SAMW circulation between H1 and YD. These changes in combination with other proxy records from the same site suggested a strong northward flow of high pCO2 and nutrient-enriched AAIW/SAMW during H1 and YD, synchronous with the changes in the proxy records from the eastern Pacific equatorial upwelling region and even off Baja California. Our proxy evidence supports earlier assumptions about the far-reaching effects of AAIW/SAMW, which most likely increased outgassing of oceanic CO_2 in the eastern equatorial Pacific upwelling region[6]. Deglacial changes in our AAIW/SAMW temperature, salinity and current speed reconstructions were related to poleward shifted and strengthened SWW, which shaped the evolution and hence the properties of Southeast Pacific AAIW/SAMW.

Methods
Analysis of benthic foraminiferal stable isotopes ($\delta^{18}O$ and $\delta^{13}C$), Mg/Ca, and Ba/Ca

For Mg/Ca and stable isotope analysis on benthic foraminifer *Uvigerina peregrina* we mostly used 20 cm³ of bulk sediment which was increased to 100 cm³ in several cases during the last 20 kyrs because of lack of enough specimens. Bulk samples from Site 1233 were freeze-dried, wet sieved over a 63 μm sieve and dried in an oven at 40 °C. We then carefully selected benthic foraminifers from the >250 μm fraction

size using a stereo microscope. For Elemental analysis (Mg/Ca, Ba/Ca) ~7–20 specimens were selected and gently crushed between glass plates. If the sample material was ~ >15 specimens, the crushed sample was separated into 2/3 used for Elemental analysis and into 1/3 which was used for stable isotope measurements. In cases when the sample material was smaller, 2-3 specimens were separated from the sample and used for stable isotope analysis. Stable isotope analyses were performed at GEOMAR Helmholtz Centre for Ocean Research Kiel on a Thermo Scientific MAT 253 with a Kiel IV Carbonate device. Standard Deviations (Analytical Precision 1σ) of Bremen standards measured during the sessions ($n = 73$) was ~0.04 ‰ for $\delta^{13}C$ and ~0.09‰ for $\delta^{18}O$. Crushed samples for elemental analysis were cleaned according to standard cleaning procedure[53] (including reductive step with hydrazine) before analysis on a VARIAN 720–ES Axial ICP-OES at GEOMAR Helmholtz Centre for Ocean Research Kiel. Spectral lines for Mg/Ca ratios were 279 nm and 370 nm, and for Ba 455 nm. To monitor any remaining contamination source for the Mg/Ca (Ba/Ca) ratios through the presence of silicates and/or Mn-Fe oxyhydroxide coatings, Al (167 nm), Fe (238 nm), and Mn (257 nm) were measured. Al/Ca and Mn/Ca ratios were on average low and near detection limits and Fe/Ca ratios showed a median value of 0.1 mmol/mol indicating effective cleaning. However, when Al/Ca ratios were greater than >0.1 mmol/mol and were accompanied by relatively high Mg/Ca ratios we discarded these samples (including Ba/Ca values) as this might be an indication of contamination with terrigenous material[53]. Mostly, these samples also showed higher Fe/Ca ratios (>0.1 mmol/mol). In one case, we decided to discard a sample based on high Fe/Ca. To correct a drift during the measurement sessions, the ECRM 752-1 standard was measured repeatedly. Blanks were inserted every 15th sample to monitor any external contamination. On average, analytical precision (1σ) for Mg/Ca ratios was -0.04 mmol/mol.

Calculation of Benthic temperatures, $\delta^{18}O_{seawater}$ and ice volume corrected seawater values ($\delta^{18}O_{IVC-seawater}$)

Bottom water temperatures were reconstructed using the core top based equation[54]: Mg/Ca= 0.074 (±0.004) x T + 0.81 (±0.05) which translates into a temperature error of - ±0.9 °C when applying our analytical precision of Mg/Ca analyses. We chose this equation as it provides the best fit of our core top benthic Mg/Ca-derived temperatures of on average 3.8 °C (7 data points within the last 5.3 kyrs) with modern observed temperatures of 4.5 °C at 830 m water depth near Site 1233 (ref. 55). It is known that the carbonate ion saturation of sea waters changed during the last deglaciation and is different between water masses and that this can affect benthic foraminiferal Mg/Ca ratios either during the precipitation process or post-depositional through calcite dissolution[54,56]. However, as has been shown, Mg/Ca ratios of *Uvigerina peregrina* are practically unaltered by these changes[54,56] supporting the robustness of our benthic Mg/Ca-derived temperatures.

Before calculating $\delta^{18}O_{seawater}$ and ice volume corrected seawater values ($\delta^{18}O_{IVC-seawater}$) which serve as an approximation for past changes in salinities, the benthic $\delta^{18}O$ record was interpolated because unfortunately, not all our Mg/Ca data were covered by $\delta^{18}O$ data points due to lack of sample material. Interpolation between measured $\delta^{18}O$ values were in the range of a few hundred years, and only once during the Holocene reach about 1 kyr. Due to interpolation between such short time intervals, we assume that the values are robust. $\delta^{18}O_{seawater}$

values were then calculated using an established equation[57]: T = 16.9 − 4.38 · ($\delta^{18}O_{foram}$- $\delta^{18}O_{seawater}$) + 0.1 · ($\delta^{18}O_{foram}$ - $\delta^{18}O_{seawater}$)^2 after adding 0.27 ‰ for adjusting to the SMOW scale[58]. Finally, values were corrected for changes in global ice volume to calculate $\delta^{18}O_{IVC-seawater}$ values. Here a high-resolution estimation of global ice volume change was used which is based on multiple observations of sea level changes over the last 35 kyrs[59]. On average, the propagated error for our $\delta^{18}O_{seawater}$ values is ∼ ± 0.26‰ and we estimate a similar error for our $\delta^{18}O_{IVC-seawater}$ values as we used the high-resolution and accurate ice volume estimation[59].

Grain size analyses and sortable silt mean grain size ($\overline{SS}$) as paleocurrent proxy

For grain size analyses we used approx. 700–750 mg from the freeze-dried bulk sediment (20 cm³), and then chemical removal steps of organic material and calcium carbonate followed[60,61]. To minimize any possible contamination with dust particles during removal steps, we decided to work under a laminar flow cabinet. Biogenic silica was not removed as opal concentrations were on average 3.7% (max. value of 5.2%) within the studied time interval[21,62] and therefore estimated as negligible[60]. Organic material was removed by adding 20 mL H_2O_2 (35%) at about 70 °C for 6 h or until no further reaction took place. $CaCO_3$ was removed by adding 10 ml HCl (10%) to 100 ml MilliQ water at about 90 °C for a few minutes. Subsequently, the acid sample solution was removed by repeated dilution with MilliQ water and decantation. Visual inspection of some samples after the removal steps with a microscope could not reveal any biogenic material. Finally, sample material was ultrasonicated and stored in a 0.02 M Polyphosphate solution. Before analysis, samples were again shortly ultrasonicated, filtered over a 100 μm membrane and analyzed on a Beckman Coulter Counter Multisizer 4e with an aperture tube of 100 μm at Pontifical Catholic University of Chile.

$\overline{SS}$ was then calculated according to the equation[63,64]: $\overline{SS} = \frac{1}{V} \sum_{i=190}^{400} (V_i \cdot d_i)$ Where i is the size bin reaching from 190 = 10.02 μm to 400 = 59.75 μm. (The used grain size scale is justified as no grains were detected within 59.75 μm and 63 μm. V_i is the differential volume at the ith size bin, and d_i is mid-size of the ith size bin, and V is the total volume between $i = 190$ and $i = 400$. Because it has been shown that only a few data counts of the coarse end of the Sortable Silt scale can alter the $\overline{SS}$ result through their disproportional high weights compared to the small grain numbers[64], every sample was measured 2–6 times and an average value was calculated showing a standard deviation (1σ) of on average ∼0.5 μm (150 samples). Additionally, all raw values of repeated analyses of the same samples were monitored to check consistency between single measurements. In 20 samples, we discarded single grain counts (1–4) in the coarse fraction (∼30–60 μm) as they were not represented in the repeated analyses. Before rejecting these single grain counts, these samples usually showed an anomalous high standard deviation between 1.2 μm and 2.5 μm. Mismatches between repeated analyses of the same samples might have been caused by different errors. One might be the possibility that air bubbles were occasionally trapped within the system during measuring and were erroneously counted as grains. The other is the described phenomena of coincidence correction of measuring single grains, which can lead to artificial counts of grains caused by the software[64].

Age model

For an initial age control of Site 1233 we used published age control tie points during the Holocene based on tuning high-resolution Ca and magnetic susceptibility records to nearby ¹⁴C dated core GeoB3313-3 (Supplementary Fig. 4; ref. [65]). For the period 8.7–32.8 ka BP we used 21 existing mixed planktic foraminiferal ¹⁴C AMS age control points[46,65–67]. These ¹⁴C AMS age datums were originally calibrated based on different curves e.g., CALPAL 2004 January calibration curve (www.calpal.de), INTCAL04 (ref. [68]), and Fairbanks0107 (ref. [69]). As all these calibration curves are now outdated, we updated the original ¹⁴C AMS age datums with Calib 8.20 software[70] using the current calibration curve for the Southern Hemisphere[71] (SHCal20; see Supplementary Table 1). Evidence from detailed tephrostratigraphy from southward located MD07-3088 indicates that reservoir ages most likely have considerably changed during the studied time-period[24,72]. As a detailed tephros-tratigraphic study does not exist from Site 1233, we applied variable reservoir ages for the surface ocean using a model simulation[73] and subtracted these from the initial datums before calibration (see Supplementary Table 1). Simulated average reservoir ages close by Site 1233 (41°S; 75°W) with a temporal resolution of 1 kyr were used for the critical time between 11 and 25 ka BP, and this resolution was lowered to 5 kyr for the Holocene and the remaining glacial period[73]. Subsequently, a 3-point moving average smooth was calculated. Then, uncalibrated atmospheric ¹⁴C ages were determined for these simulated sea surface reservoir ages and applied to uncalibrated ¹⁴C age datums from Site 1233. The obtained results were compared with the sea surface reservoir age from an identified tephra layer (Lepué Tephra) at Site 1233 with a basal depth of 14.80 mcd, which eruption could be dated using land deposits indicating a ¹⁴C age (BP) of ∼9588 years[74]. Interpolation between planktic foraminiferal radiocarbon ¹⁴C ages (BP) at Site 1233 gives a marine age of ∼10.07 ka BP for this tephra layer, resulting in a difference of 481 years compared with the land deposits, which is in accordance with the used simulated sea surface reservoir age of 554 years for this time (see Supplementary Table 1). The maximum difference between our used model-based surface reservoir age estimations[73] and these proposed for site MD07-3088 (ref. [24]) is ∼400 years. Compared to previous reported age models from the same Site[46,65–67] our revised age model has a maximum difference of ∼1000 years during the deglaciation (Supplementary Fig. 4). As during the critical time period between 8 and 30 ka BP, there is every 1.1 kyrs a ¹⁴C AMS tie point, and the simulated surface reservoir ages were confirmed by one tephra layer, we assess the age model as robust. Indirect support for the updated age control comes from the timely match of our benthic $\delta^{18}O$ and an Antarctic $\delta^{18}O$ ice core stack[47] (Fig. 4a).

DCESS model simulation

The DCESS Earth system model[75] features modules for the atmosphere, ocean, ocean sediment, land biosphere and lithosphere, calibrated and tested against Earth system data and against output from more complex models. The model consists of one hemisphere, divided by 52° latitude into a low-mid latitude and a high latitude zone. The atmosphere module considers radiation balance, meridional transport of heat and water vapor between low-mid latitude and high latitude zones, and heat and gas exchange with the ice-free part of the ocean. Gases considered are carbon dioxide and methane for all three carbon isotopes, nitrous oxide and oxygen.

The model ocean is 270° wide, extends from the equator to 70° latitude and covers 70.5% of the Earth surface. Each ocean sector has 55 vertical layers with 100 m resolution. An ocean sediment sector is assigned to each ocean layer with widths taken from observed depth distributions. The ocean module has prescribed circulation and mixing. Model ocean tracers are temperature, salinity, oxygen isotope in water, phosphate, dissolved inorganic carbon for all three carbon isotopes, and alkalinity. Biogenic production of particulate organic matter depends on surface layer phosphate availability but with lower efficiency in the high latitude zone, due for example to iron limitation. The calcite to organic carbon rain ratio depends on surface layer temperature and carbonate ion concentration[76].

The semi-analytical, ocean sediment module considers calcium carbonate dissolution and oxic and anoxic organic matter reminer-alization. The sediment is composed of calcite, non-calcite mineral and reactive organic matter. The land biosphere module considers leaves,

wood, litter and soil. Net primary production depends on atmospheric carbon dioxide concentration and remineralization rates in the litter and soil depend on mean atmospheric temperatures. Methane production is a small fraction of the soil remineralization. This module has been extended to include three dynamically varying vegetation zones and a permafrost component[77]. The lithosphere module considers outgassing, weathering of carbonate and silicate rocks and weathering of rocks with old organic carbon and phosphorus.

For the simulation presented here we applied a approach[77] for the last glacial termination that was updated to better represent dust-climate feedbacks[78]. For the period 25 ka BP to the present, we prescribed albedo forcing from changing ice sheet size as well as dust radiative forcing and iron fertilization of high latitude ocean biota as described in the above references.

We found agreement with observed low last glacial atmospheric $p\text{CO}_2$ for the prescribed 25 ka BP forcing and with vertical exchange coefficient in the high latitude ocean (kvHL) above 1000 m reduced by 30% relative to pre-industrial levels (as calibrated before[75]) and kvHL below 1000·2000 m set to low values of the low-mid latitude ocean. Depth-dependent kvHL in the model last glacial generates a model analogy to isolated deep water in the Southern Ocean at that time. This is meant to emulate the effects of some combination of weakened or equatorward-shifted SWW and increased stratification through brine-induced effects as have been suggested in various studies[31,48,79,80]. This led to significantly increased deep ocean storage of ^{13}C-depleted, dissolved inorganic carbon from remineralization of organic matter raining down from the ocean surface layer. In addition to the above mentioned forcing we also varied over time the size and distribution of kvHL to simulate storage/release of deep ocean carbon from/to the upper ocean and atmosphere (Supplementary Fig. 2). For the H1 and YD periods, we increased kvHL over all or most high latitude ocean depths to at or near preindustrial levels to emulate increased Southern Ocean upwelling drawn from greater depths as well as increased vertical exchange as would result from stronger SWW during these periods.

Data availability
The proxy data generated in this study have been deposited in the World Data Center for Paleoclimatology (WDC Paleo) under accession code: https://www.ncei.noaa.gov/access/paleo-search/study/40139.

Code availability
Results from the model simulation is available at www.dcess.dk.

References
1. Sabine, C. L. et al. The oceanic sink for anthropogenic CO2. *Science* **305**, 367–CO371 (2004).
2. McCartney, M. S. Subantarctic Mode Water. In: Angel, M. (Ed.), A Voyage of Discovery. Pergamon, Oxford, pp. 103–119 (1977).
3. Sarmiento, J., Gruber, N., Brzezinski, M. A. & Dunne, J. P. High-latitude controls of thermocline nutrients and low latitude biological productivity. *Nature* **427**, 56–60 (2004).
4. Resplandy, L., Bopp, L., Orr, J. C. & Dunne, J. P. Role of mode and intermediate waters in future ocean acidification: analysis of CMIP5 models. *Geophys. Res. Lett.* **40**, 3091–3095 (2013).
5. Ishii, M. et al. Ocean acidification from below in the tropical pacific. *Glob. Biogeochemical Cycles* **34**, e2019GB006368 (2020).
6. Martínez-Botí, M. A. et al. Boron isotope evidence for oceanic carbon dioxide leakage during the last deglaciation. *Nature* **518**, 219–222 (2015).
7. Takahashi, T. et al. Climatological mean and decadal change in surface ocean pCO2, and net sea-air CO2 flux over the global oceans. *Deep-Sea Res. I* **56**, 2075–2076 (2009).
8. Köhler, P. et al. A 156 kyr smoothed history of the atmospheric greenhouse gases CO2, CH4, and N2O and their radiative forcing. *Earth Syst. Sci. Data* **9**, 363–387 (2017).
9. Clark, P. U. et al. Global climate evolution during the last deglaciation. *Proc. Natl Acad. Sci. USA* **109**, 1134–1142 (2012).
10. Anderson, R. F. et al. Wind-driven upwelling in the Southern ocean and the deglacial rise in atmospheric CO2. *Science* **13**, 1443–1448 (2009).
11. Skinner, L. C. et al. Ventilation of the Deep Southern Ocean and Deglacial CO2 Rise. *Science* **328**, 1147–1151 (2010).
12. Bova, S. C. et al. Links between eastern equatorial Pacific stratification and atmospheric CO2 rise during the last deglaciation. *Paleoceanography* **30**, 1407–1424 (2015).
13. Oppo, D. W. & Fairbanks, R. G. Carbon isotope composition of tropical surface water during the past 22,000 years. *Paleoceanography* **4**, 333–351 (1989).
14. Ninnemann, U. S. & Charles, C. D. Regional differences in Quaternary subantarctic nutrient cycling: Link to intermediate and deep water ventilation. *Paleoceanography* **12**, 560–567 (1997).
15. Spero, H. J. & Lea, D. W. The Cause of Carbon Isotope Minimum Events on Glacial Terminations. *Science* **296**, 522–525 (2002).
16. Marchitto, T. M. et al. Marine Radiocarbon Evidence for the Mechanism of Deglacial Atmospheric CO$_2$ Rise. *Science* **316**, 1456–1459 (2007).
17. Calvo, E. et al. Eastern Equatorial Pacific productivity and related-CO$_2$ changes since the last glacial period. *Proc. Natl Acad. Sci. USA* **108**, 5537–5541 (2011).
18. Lindsay, C. M. et al. The surface expression of radiocarbon anomalies near Baja California during deglaciation. *Earth Planet. Sci. Lett.* **422**, 67–74 (2015).
19. Lindsay, C. M. et al. New constraints on deglacial marine radiocarbon anomalies from a depth transect near Baja California. *Paleoceanography* **31**, 1103–1116 (2016).
20. Haddam, N. A. et al. Ventilation and expansion of intermediate and deep waters in the Southeast Pacific during the last termination. *Paleoceanogr. Paleoclimatol.* **35**, e2019PA003743 (2020).
21. Muratli, J. et al. Increased glacial-age ventilation of the Chilean margin by Antarctic Intermediate Water. *Nat. Geosci.* **3**, 23–26 (2010).
22. Martínez Fontaine, C. et al. Ventilation of the Deep Ocean Carbon Reservoir During the Last Deglaciation: Results From the Southeast Pacific. *Paleoceanogr. Paleoclimatol.* **34**, 2080–2097 (2019).
23. De Pol-Holz, R. et al. No signature of abyssal carbon in intermediate waters off Chile during deglaciation. *Nat. Geosci.* **3**, 192–195 (2010).
24. Siani, G. et al. Carbon isotope records reveal precise timing of enhanced Southern Ocean upwelling during the last deglaciation. *Nat. Comm.* **4**, 2758 (2013).
25. Bostock, H. C. et al. Reviewing the circulation and mixing of Antarctic Intermediate Water in the South Pacific using evidence from geochemical tracers and Argo float trajectories. *Deep Sea Res. Part I Oceanogr.* **73**, 84–98 (2013).
26. Hanawa, K. & Talley, L. D. Mode Waters. *Ocean Circulation and Climate*, 373–386, Eds., Siedler, G. & Church, J., International Geophysics Series (Academic Press 2001).
27. Reyes-Macaya, D. et al. Isotopic characterization of water masses in the Southeast Pacific region: Paleoceanographic implications. *J. Geophys. Res. Oceans* **127**, e2021JC017525 (2022).
28. Sloyan, B. M. & Rintoul, S. R. Circulation, Renewal, and Modification of Antarctic Mode and Intermediate Water. *J. Phys. Oceanogr.* **31**, 1005–1030 (2001).
29. Schmitt, J. et al. Carbon Isotope Constraints on the Deglacial CO$_2$ Rise from Ice Cores. *Science* **336**, 711–714 (2012).
30. Shao, J. et al. The atmospheric bridge communicated the δ^{13}C decline during the last deglaciation to the global upper ocean. *Clim* **17**, 1507–1521 (2021).
31. Menviel, L. et al. Southern Hemisphere westerlies as a driver of the early deglacial atmospheric CO2 rise. *Nat. Comm.* **9**, 2503 (2018).

32. Farmer, E. C. et al. Corroborating ecological depth preferences of planktonic foraminifera in the tropical Atlantic with the stable oxygen isotope ratios of core top specimens. *Paleoceanography* **22**, PA3205 (2007).

33. Bradtmiller, L. I., Anderson, R. F., Fleisher, M. Q. & Burckle, L. H. Diatom productivity in the equatorial Pacific Ocean from the last glacial period to the present: a test of the silicic acid leakage hypothesis. *Paleoceanography* **21**, PA4201 (2006).

34. Nie, X., Gao, S., Wang, F., Chi, J. & Qu, T. Origins and pathways of the Pacific Equatorial Undercurrent identified by a simulated adjoint tracer. *J. Geophys. Res.: Oceans* **124**, 2331–2347 (2019).

35. Rafter, P. A. & Sigman, D. M. Spatial distribution and temporal variation of nitrate nitrogen and oxygen isotopes in the upper equatorial Pacific ocean. *Limnol. Oceanogr.* **61**, 14–31 (2016).

36. Toggweiler, J. R., Druffel, E. R. M., Key, R. M. & Galbraith, E. D. Upwelling in the ocean basins north of the ACC: 1. On the upwelling exposed by the surface distribution of Δ14 C. *J. Geophys. Res. Oceans* **124**, 2591–2608 (2019).

37. Rodgers, K. B. et al. Low-latitude mesopelagic nutrient recycling controls productivity and export. *Nature* **632**, 802–807 (2024).

38. Chase, Z., Anderson, R. F., Fleisher, M. Q. & Kubik, P. W. Accumulation of biogenic and lithogenic material in the Pacific sector of the Southern Ocean during the past 40,000 years. *Deep-Sea Res., Part 2, Top. Stud. Oceanogr.* **50**, 799–832 (2003).

39. Pahnke, K. & Zahn, R. Southern Hemisphere Water Mass Conversion Linked with North Atlantic Climate Variability. *Science* **307**, 1741–1746 (2005).

40. Li, L., Liu, Z., Zhu, C., He, C. & Otto-Bliesner, B. Shallowing glacial Antarctic Intermediate Water by changes in sea ice and hydrological cycle. *Geophys. Res. Lett.* **48**, e2021GL094317 (2021).

41. Hain, M. P., Sigman, D. M. & Haug, G. H. Shortcomings of the isolated abyssal reservoir model for deglacial radiocarbon changes in the mid-depth Indo-Pacific Ocean. *Geophys. Res. Lett.* **38**, L04604 (2011).

42. Basak, C., Martin, E. E., Horikawa, K. & Marchitto, T. M. Southern Ocean source of 14C-depleted carbon in the North Pacific Ocean during the last deglaciation. *Nat. Geosci.* **3**, 770–773 (2010).

43. Zhao, N. & Keigwin, L. D. An atmospheric chronology for the glacial-deglacial eastern equatorial Pacific. *Nat. Commun.* **9**, 3077 (2018).

44. Bova, S. C., Herbert, T. D. & Altabet, M. A. Ventilation of northern and southern sources of aged carbon in the eastern equatorial Pacific during the Younger Dryas rise in atmospheric CO2. *Paleoceanogr. Paleoclimatol.* **33**, 1151–1168 (2018).

45. Fuhr, M. et al. Tracing Water Mass Mixing From the Equatorial to the North Pacific Ocean With Dissolved Neodymium Isotopes and Concentrations. *Front. Mar. Sci.*, **7** https://doi.org/10.3389/fmars. 2020.603761 (2020).

46. Lamy, F. et al. Modulation of the bipolar seesaw in the Southeast Pacific during Termination 1. *Earth Planet. Sci. Lett.* **259**, 400e413 (2007).

47. Buizert, C. et al. Abrupt ice-age shifts in southern westerly winds and Antarctic climate forced from the north. *Nature* **563**, 681–685 (2018).

48. Gray, W. R. et al. Poleward shift in the Southern Hemisphere westerly winds synchronous with the deglacial rise in CO2. *Paleoceanogr. Paleoclimatol* **38**, e2023PA004666 (2023).

49. Roberts, J. et al. Deglacial changes in flow and frontal structure through the Drake Passage. *Earth Planet. Sci. Lett.* **474**, 397–408 (2017).

50. Sallée, J. et al. Southern Ocean Thermocline Ventilation. *J. Phys. Oceanogr.* **40**, 509–529 (2010).

51. Keeling, R. F. & Stephens, B. B. Antarctic sea ice and the control of Pleistocene climate instability. *Paleoceanography* **16**, 112–131 (2001).

52. Abernathey, R. et al. Water-mass transformation by sea ice in the upper branch of the Southern Ocean overturning. *Nat. Geosci.* **9**, 596–601 (2016).

53. Barker, S., Greaves, M. & Elderfield, H. A study of cleaning procedures used for foraminiferal Mg/Ca paleothermometry. *Geochem. Geophys. Geosyst.* **4**, 8407 (2003).

54. Elderfield, H. et al. A record of bottom water temperature and seawater δ18O for the Southern Ocean over the past 440 kyr based on Mg/Ca of benthic foraminiferal Uvigerina spp. *Quat. Sci. Rev.* **29**, 160–169 (2010).

55. Locarnini, R. A. et al. World Ocean Atlas 2013, Volume 1: Temperature. S. Levitus, Ed., A. Mishonov Technical Ed.; NOAA Atlas NESDIS **73**, 40 pp (2013).

56. Elderfield, H. et al. Calibrations for benthic foraminiferal Mg/Ca paleothermometry and the carbonate ion hypothesis. *Earth Planet Sci. Lett.* **250**, 633–649 (2006).

57. Shackleton, N. J. Attainment of isotope equilibrium between ocean water and the benthonic foraminiferal genus Uvigerina. Isotopic changes in the ocean during the last glacial. *Cent. Nat. Rech. Sci. Colloq. Int.* **219**, 203 (1974).

58. Hut, G. Consultants' group meeting on stable isotope reference samples for geochemical and hydrological investigations. Int. Atomic Energy Agency, Vienna (1987).

59. Lambeck, K. et al. Sea level and global ice volumes from the Last Glacial Maximum to the Holocene. *Proc. Natl Acad. Sci. U. S. A* **111**, 15296–15303 (2014).

60. Mc Cave, I. et al. Sortable silt and fine sediment size/composition slicing: parameters for palaeocurrent speed and palaeoceanography. *Paleoceanography* **10**, 593–610 (1995).

61. Mulitza, S. et al. Sahel megadroughts triggered by glacial slowdowns of Atlantic meridional overturning. *Paleoceanography* **23**, PA4206 (2008).

62. Chase, Z., McManus, J., Mix, A. C. & Muratli, J. Southern-ocean and glaciogenic nutrients control diatom export production on the Chile margin. *Quat. Sci. Rev.* **99**, 135–145 (2014).

63. Tegzes, A. D. et al. The role of the northward-directed (sub)surface limb of the Atlantic Meridional Overturning Circulation during the 8.2 ka event. *Clim* **10**, 1887–1904 (2014).

64. Tegzes, A. D., Jansen, E. & Telford, R. J. Which is the better proxy for paleo-current strength: Sortable-silt mean size (ss) or sortable-silt mean grain diameter (dSS)? A case study from the Nordic Seas. *Geochem. Geophys. Geosyst.* **16**, 3456–3471 (2015).

65. Kaiser, J., Lamy, F. & Hebbeln, D. A 70-kyr sea surface temperature record off southern Chile (Ocean Drilling Program Site 1233). *Paleoceanography* **20**, PA4009 (2005).

66. Lamy, F. et al. Antarctic timing of surface water changes off Chile and Patagonian Ice Sheet response. *Science* **304**, 1959e1962 (2004).

67. Kaiser, J. et al. Links between Patagonian Ice Sheet fluctuations and Antarctic dust variability during the last glacial period (MIS 4-2). *Quat. Sci. Rev.* **29**, 1464–1471 (2010).

68. Reimer, P. J. et al. INTCAL04 terrestrial radiocarbon age calibration, 0-26 cal kyr BP. *Radiocarbon* **46**, 1029–1058 (2004).

69. Fairbanks, R. G. Radiocarbon calibration curve spanning 0 to 50,000 years BP based on paired 230Th/234U/238U and 14C dates on pristine corals. *Quat. Sci. Rev.* **24**, 1781–1796 (2005).

70. Stuiver, M. & Reimer, P. J. CALIB rev. 8. *Radiocarbon* **35**, 215–230 (1993).

71. Hogg, A. G. et al. SHCal20 Southern Hemisphere Calibration, 0–55,000 Years cal BP. *Radiocarbon* **62**, 759–778 (2020).

72. Carel, M., Siani, G. & Delpech, G. Tephrostratigraphy of a deep-sea sediment sequence off the south Chilean margin: New insight into the Hudson volcanic activity since the last glacial period. *J. Volcanol. Geotherm. Res.* **208**, 99–111 (2011).

73. Butzin, M., Köhler, P. & Lohmann, G. Marine radiocarbon reservoir age simulations for the past 50,000 years. *Geophys. Res. Lett.* **44**, 8473–8480 (2017).

74. Alloway, B. V. et al. Stratigraphy, age and correlation of Lepue Tephra: a widespread c. 11000 cal a BP marker horizon sourced from the Chaiten Sector of southern Chile. *J. Quat. Sci.* **32**, 795–829 (2017).

75. Shaffer, G., Olsen, S. M. & Pedersen, J. O. P. Presentation, calibration and validation of the low-order, DCESS Earth System Model (Version 1). *Geoscientific Model Dev.* **1**, 17–51 (2008).

76. Shaffer, G., Huber, M., Rondanelli, R. & Pepke Pedersen, J. O. Deep time evidence for climate sensitivity increase with warming. *Geophys. Res. Lett.* **43**, 6538–6545 (2016).

77. Eichinger, R. et al. An improved land biosphere module for use in the DCESS Earth system model (version 1.1) with application to the last glacial termination. *Geoscientific Model Dev.* **10**, 3481–3498 (2017).

78. Shaffer, G. & Lambert, F. In and out of glacial extremes by way of dust–climate feedbacks. *Proc. Natl Acad. Sci. Usa.* **115**, 2026–2031 (2018).

79. Bouttes, N., D. Paillard, D. & Roche, D. M. Impact of brine-induced stratification on the glacial carbon cycle. *Clim* **6**, 575–589 (2010).

80. Toggweiler, J. R., Russell, J. L. & Carson, S. R. Midlatitude westerlies, atmospheric CO2, and climate change during the ice ages. *Paleoceanography* **21**, PA2005 (2006).

81. Schlitzer, R. Ocean Data View, http://odv.awi.de (2020).

82. Zweng, M. M. et al. World Ocean Atlas 2013, Volume 2: Salinity. Levitus, S. Ed., Mishonov, A. Technical Ed.; NOAA Atlas NESDIS 74, **39** (2013).

83. Garcia, H. E. et al. World Ocean Atlas 2013, Volume 3: Dissolved Oxygen, Apparent Oxygen Utilization, and Oxygen Saturation. Levitus, S. Ed., Mishonov, A. Technical Ed.; NOAA Atlas NESDIS 75, **27** (2013).

Acknowledgements

Author contributions

C.K. conceptualized this study, led the writing of the manuscript, the analyzing and interpretation of the data. D.N., F.B., G.S., and F.L. were involved in the interpretation of the data and in writing. D.N. and F.B. contributed to the analysis of the data. G.S. provided the model simulation results.

Competing interests

The authors declare no competing interests.

Additional information

Supplementary information The online version contains supplementary material available at https://doi.org/10.1038/s41467-025-60551-5.

Correspondence and requests for materials should be addressed to Cyrus Karas.

Peer review information *Nature Communications* thanks Masao Ishii, Juan Muglia and the other, anonymous, reviewer(s) for their contribution to the peer review of this work. A peer review file is available.

Reprints and permissions information is available at http://www.nature.com/reprints

Publisher's note Springer Nature remains neutral with regard to jurisdictional claims in published maps and institutional affiliations.